PROCEEDINGS OF SCIENCE

PoS(ICRC2023)542

Electron acceleration at oblique supernova remnant shocks

Artem Bohdan,[a,b] **Karol Fulat,**[c,*] **Paul J. Morris,**[d] **Martin S. Weidl,**[a] **Michelle Tsirou**[d] **and Martin Pohl**[c,d]

[a] *Max-Planck-Institut für Plasmaphysik, Boltzmannstr. 2, DE-85748 Garching, Germany*
[b] *Excellence Cluster ORIGINS, Boltzmannstr. 2, DE-85748 Garching, Germany*
[c] *Institute of Physics and Astronomy, University of Potsdam, D-14476 Potsdam, Germany*
[d] *Deutsches Elektronen-Synchrotron DESY, Platanenallee 6, 15738 Zeuthen, Germany*

E-mail: `artem.bohdan@ipp.mpg.de`

Supernova remnants are known as efficient particle accelerators due strong non-thermal radiation emitted by self-produced relativistic electrons, protons and ions. Diffusive shock acceleration (DSA) operating in these shocks is believed to be responsible for acceleration of high energy particles. In order for DSA to work, a particle should have a gyroradus larger than the finite width of a shock. Therefore, thermal electrons require a substantial pre-acceleration before they can cross the shock within one gyration and be accelerated via DSA. Here we use particle-in-cell simulations to study microphysics of electron acceleration in oblique high Mach number shocks. In this case, fast electrons can escape to the shock upstream, modifying the shock foot to a region called the electron foreshock. We find that the observed electron-beam instabilities agree very well with the predictions of a linear dispersion analysis: the electrostatic electron-acoustic instability dominates in the outer region of the foreshock, while the denser electron beams in the inner foreshock drive the gyroresonant oblique-whistler instability. Both foreshock instabilities play a crucial role in production of nonthermal electrons via resonant interaction and stochastic scattering. As a result, the downstream spectrum of electrons is characterized with a pronounced nonthermal tail, making the injection of electrons into DSA possible, thus enabling electron acceleration to higher energies.

38th International Cosmic Ray Conference (ICRC2023)
26 July - 3 August, 2023
Nagoya, Japan

---

[*] Speaker

1. Introduction

Supernova explosions are known to interact with the interstellar medium, generating high Mach number shocks associated with intense nonthermal emission. Notably, electrons play a significant role in producing nonthermal radiation in various bands, including radio, X-ray, and γ-rays. The process responsible for accelerating these high-energy electrons is believed to be diffusive shock acceleration (DSA), a first-order Fermi acceleration mechanism occurring in the shock transition region. However, DSA requires pre-acceleration or injection of particles from the thermal pool, a task more challenging for electrons due to their lower mass compared to ions.

To study electron-scale phenomena responsible for pre-acceleration, we employ high-resolution two-dimensional particle-in-cell (PIC) simulations, providing a fully self-consistent treatment of the electron scales. In the high Mach number regime, the dissipation of upstream ion kinetic energy cannot rely solely on resistive (Joule) dissipation. Instead, a substantial portion of the incoming ions is reflected back upstream, giving rise to various instabilities in the shock transition. However, the obliquity angle, $\theta_{\rm Bn}$, between the shock normal and upstream magnetic field, significantly influences shock behavior and ability of particles escape the shock to form the so-called foreshock region. Oblique shocks permit electron escape or reflection along the upstream magnetic field lines creating the electron foreshock.

In this proceedings, we present a comprehensive summary of our recent research on oblique high-Mach-number shocks [1–3]. We outline the most important results, including the characterization of electron foreshock structures, the underlying mechanism responsible for electron reflection, the nonlinear whistler structures, and the modified stochastic shock drift acceleration mechanism.

2. Simulation setup

The work presented here makes use of code adapted from TRISTAN [5] which allows us to study fully relativistic shocks while tracking 2-spatial and all 3 velocity components (2D3V) of individual plasma particles [6]. This implementation of the code provides the ability to trace individual particles, where we can track the components of their velocities and local fields, facilitating a detailed analysis of the electron acceleration microphysics.

In this study, we employ a reflecting wall setup to generate a shock by reflecting an incoming plasma beam from a conducting wall positioned at $x = 0$ within our simulation box (Fig. 1). The reflection involves a velocity transformation $v_x \rightarrow -v_x$, while v_y and v_z remain unaltered.The upstream plasma is initialized with a bulk velocity of $\boldsymbol{v}_{\rm \bf ups} = -0.2c\ \hat{\boldsymbol{x}}$. This upstream plasma is initialized with a uniform large-scale magnetic field with a field orientation described by the obliquity angle, $\theta_{\rm Bn}$ and angle relative to the simulation plane, ϕ, such that $\boldsymbol{B_0} = B_0(\cos\theta_{\rm Bn}, \sin\theta_{\rm Bn}\cos\phi, \sin\theta_{\rm Bn}\sin\phi)$ where $\theta_{\rm Bn} = 60^\circ$ and $\phi = 90^\circ$. To eliminate Larmor gyration of upstream particles associated with the bulk motion, a motional electric field $\boldsymbol{E} = -\boldsymbol{v}_{\rm \bf ups} \times \boldsymbol{B_0}$ is initialized. The adiabatic index is set to $\gamma = 5/3$, resulting in a shock compression ratio of $r \approx 4$, leading to a shock velocity of $v_{\rm sh} \simeq 0.264c$ in the upstream rest frame. This sets the Alfvénic and sonic Mach numbers as $M_A \approx 30$ and $M_s \approx 32.5$, which are defined in the upstream reference frame. The plasma beta value, which denotes the thermal-to-magnetic energy density ratio in the upstream region is $\beta = 1$. The ion-to-electron mass ratio is set to $m_i/m_e = 50$.

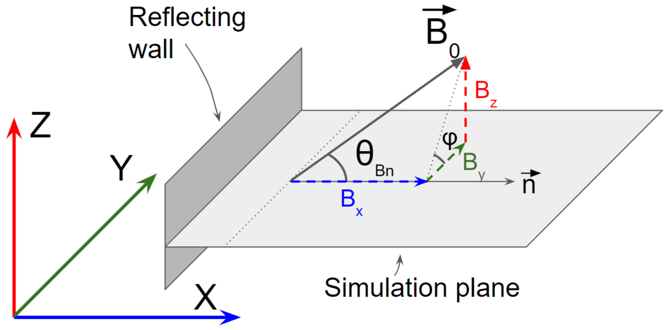

Figure 1: Simulation setup.

To ensure adequate resolution of all important timescales in our simulation, we adopt a simulation timestep of $\delta t = 1/16, \omega_{\rm pe}^{-1}$ and a resolution of $\lambda_{\rm se} = c/\omega_{\rm pe} = 8\Delta$, where Δ represents the size of one cell in our simulation grid. The number of particles per cell per species is $N_{\rm ppc} = 40$.

3. Shock structure

In oblique shocks, fast electrons can escape towards the upstream region generating electrostatic and electromagnetic waves. It leads to formation of A broader shock transition and the formation of a turbulent foreshock region that extends far into the upstream flow. The mechanism responsible for electron reflection involves shock surfing acceleration on Buneman waves [7], followed by magnetic mirroring [2]. The density of reflected electrons is approximately 1% close to the shock, and it decreases significantly farther upstream (Fig. 2(b)). The electron-density profile of the fully formed shock ($t = 18.1\Omega_{\rm i}^{-1}$), shown in Fig. 2, suggests that the simulation domain can be divided into a downstream region ($x/\lambda_{\rm se} \lesssim 1000$), the shock transition ($1000 \lesssim x/\lambda_{\rm se} \lesssim 1100$), the foreshock that can be subdivided further according to the fluctuating field components ($1100 \lesssim x/\lambda_{\rm se} \lesssim 4000$), and the upstream plasma which contains the undisturbed plasma ($x/\lambda_{\rm se} \gtrsim 4000$).

The foreshock region contains the shock-reflected electrons that stream through the background electrons with a mean velocity of $v_{\rm dr} \approx 0.9c$ along the upstream magnetic field lines. We derive parameters describing the phase-space distributions of the upstream and the reflected electrons for the selected regions of the foreshock where electrostatic and electromagnetic waves are present, and use linear dispersion analysis and PIC simulations with periodic boundaries to explore the nature of observed waves [1].

The inner foreshock region exhibits oblique waves with wavelengths between $30\lambda_{\rm se}$ and $50\lambda_{\rm se}$, characterised by significant magnetic components (Fig. 2, bottom left panel). These electromagnetic waves closely match the predictions of linear theory for the fastest-growing mode of the oblique-whistler instability. Remarkably, this electron-electron mode effectively explains the simulation results with periodic boundaries. However, differences in the parallel velocity distribution cause the spectral peak to shift from the second-order gyroresonance (as predicted by the linear model) to a larger parallel wave number, closely associated with the third-order gyroresonance.

In contrast, the outer foreshock region features a quiescent magnetic field but exhibits strong electrostatic fluctuations with a wavelength of $\lambda \approx (3-4)\lambda_{\rm se}$ (Fig. 2, bottom right panel). These electrostatic waves are attributed to the electron-acoustic instability. After modifying its linear

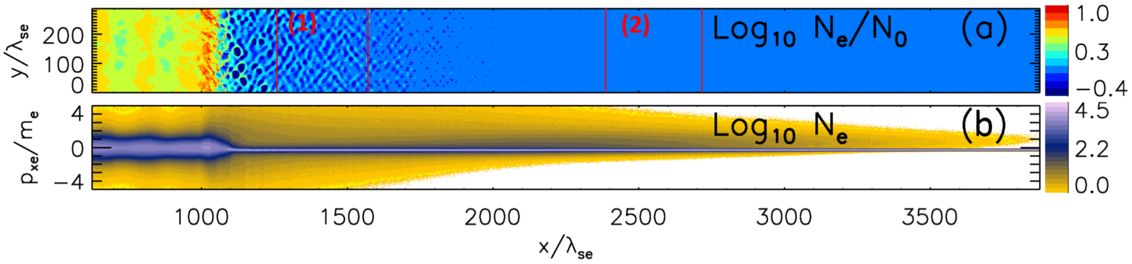

(1) Whistler waves (2) Electron-acoustic waves

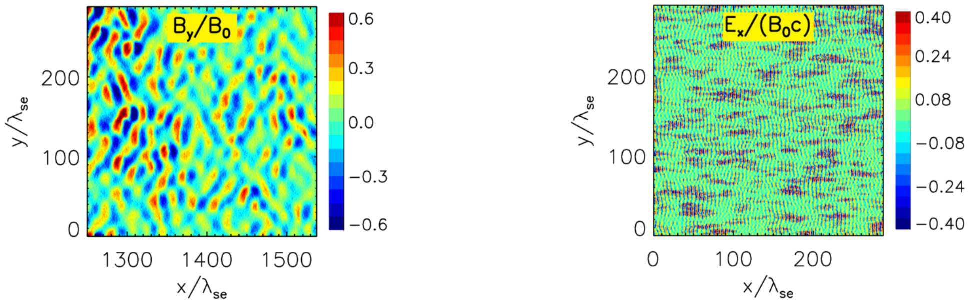

Figure 2: Map of the electron density (a), the histogram of the $x - p_x$ phase-space density electrons (b). Two bottom panel shows representative field structures of whistler (bottom left panel) and electron-acoustic (bottom right panel) waves.

dispersion relation to account for a Gaussian momentum distribution, we find excellent agreement between linear theory and the periodic-boundary-condition simulations with parallel configuration. While solving this modified dispersion relation for oblique propagation directions poses challenges, we nevertheless attribute the presence of outer-foreshock waves to the electron-acoustic instability as well.

4. Electron acceleration mechanisms

Using particle tracing data, we have identified several mechanisms contributing to electron acceleration in oblique shocks. Firstly, electrons can be deflected back upstream by electron-acoustic waves. Secondly, nonlinear whistler waves have the capability to capture reflected electrons and bring them back to the shock. Lastly, stochastic shock drift acceleration (SSDA) plays a crucial role in producing the most energetic particles.

4.1 Interaction with electron-acoustic waves

By tracing the trajectories of electrons, we have observed instances where electrons do not reach the shock transition but are still turned back upstream in the region where only electrostatic waves are present. For magnetic mirroring to be the mechanism responsible for reflection, we need a converging magnetic field, which is not present in the electrostatic foreshock. In this case, it is possible for upstream electrons to become trapped in the potential wells of the EAWs if the potential difference is sufficiently large. Acceleration by the motional electric field when trapped leads to an increase in perpendicular momenta. Subsequent acceleration by the motional electric field while trapped leads to an increase in perpendicular momenta. Additionally, electrons can experience acceleration by the on-average parallel electric field. As a result, interactions between these electrons and the EAWs can further divert them away from the shock. Note, that this process is not very efficient, because it accounts for about $\sim 1\%$ of reflected electrons in case of $\theta_{\rm Bn} \leq 45°$ and can be fully neglected in shocks which higher obliquity, e.g., $\theta_{\rm Bn} \leq 60°$ [2].

4.2 Interaction with nonlinear whistler waves

The behavior of the initial whistler wave structure can be appropriately described by linear analysis [1], at later times in the simulations they develop into non-linear wave packets, with a complex internal structure. These structures can be visible close to the shock transition in Figure 2 and they are represented as under-dense cavities where the plasma density drops to $n/n_0 \approx 0.15$.

The shock reflected electrons can interact with non-linear structures and become trapped. During this process, the electrons are carried towards the shock since they are unable to escape, until the non-linear wave encounters the shock ramp. We note that the Larmor radius of reflected electrons that are trapped by whistler waves need to be smaller in size relative to the whistler wave. Typically, the gyroradii of the reflected electrons fall in the range of $1 - 5\lambda_{\rm si}$, though they can occasionally approach $10\lambda_{\rm si}$. This comparison implies that the ratio of the reflected electron gyroradii to the radius of the non-linear structure lies within the range of $0.1 - 1$. While the magnetic field amplification associated with these non-linear structures can contract the electron gyroradii upon encountering them, it may not be sufficient to allow the non-linear structures to trap the most energetic reflected electrons. In reality, the probability of trapping is expected to decrease exponentially as the gyroradius approaches the radius of the non-linear structure, $r_{\rm nls}$, such that $P_{\rm trap} \propto \exp\left(-r_{ge}/r_{\rm nls}\right)$ [3]. However, we must also consider the fact that the size of the whistler region, from which these non-linear structures arise, grows with time [1]. We estimate that the size of this region would reach a steady state at $\Omega_{\rm i} t \approx 125$. At this time, the whistler-containing region would extend to around $2000\lambda_{\rm si}$ ahead of the shock. Within this context, we anticipate the trapping probability to increase until $\Omega_{\rm i} t \approx 125$ for all reflected electrons with gyroradii small enough to be contained by the non-linear structures.

4.3 SSDA

Another candidate acceleration mechanism in oblique shocks is shock drift acceleration (SDA) [8, 9]. This mechanism comes into play when an electron gyrates close enough to the shock ramp, causing part of its orbit to overlap with a region of enhanced magnetic field, thereby tightening its gyroradius during these intervals. The gradient in the magnetic field results in a drift effect akin to ∇B drift, with work done by the motional electric field. While SDA efficiently energizes electrons, it alone is not sufficient to account for the observed power-law spectrum and fluxes of accelerated electrons in astrophysical sources. The limitation arises because, in the original SDA theory, candidate electrons are not confined to the shock transition region where acceleration occurs, thereby limiting the efficiency of the mechanism. One way to address this limitation is by incorporating pitch angle scattering, with electrons scattering off whistlers, as observed in the Earth's bow shock [10]. To enhance the time spent in the acceleration region and consequently increase the energy gain, [11] proposed the stochastic shock drift acceleration (SSDA) mechanism, which integrates pitch angle scattering into the SDA model. Subsequent evidence of SSDA has

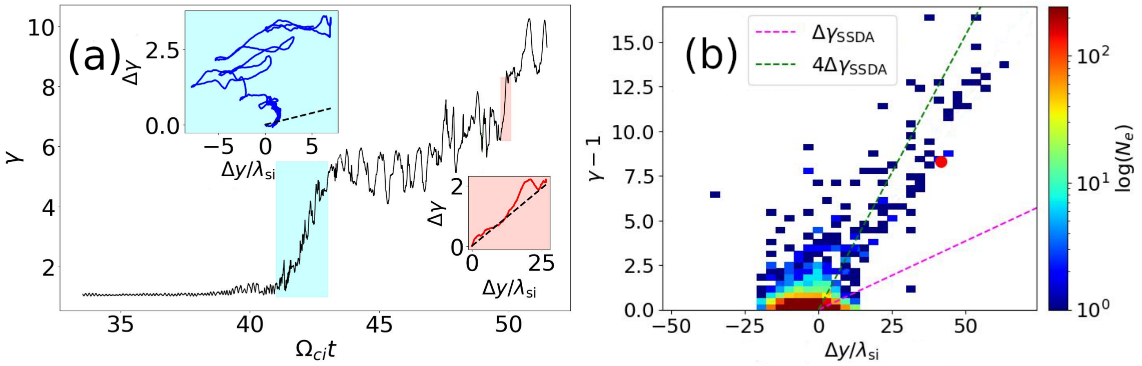

Figure 3: Panel (a): the temporal development of the kinetic energy of the sample electron. Panel (b): the change in Lorentz factor as a function of $\Delta y/\lambda_{\rm si}$ at $\Omega_{\rm i}t = 51.5$ for the traced electrons. The negative average Δy typically occurs for electrons that have passed into the downstream. The location of the sample electron is indicated by the red circle. Under the assumption that the work done to cause the acceleration comes from the motional electric field, SSDA predicts $\Delta\gamma_{\rm SSDA} \approx q_e E_{0y}\Delta y/(m_e c^2)$ (purple dashed line), the energy gain for the most energetic electrons is about 4 times greater (green dashed line).

been found in both 3D PIC simulations [12] and observations supporting electron scattering by whistler waves [13].

This picture is consistent with acceleration of the sample electron. In panel (a) of Figure 3, it can be observed that this particular electron undergoes two periods of rapid and efficient acceleration, separated by a period of relative quiescence. At approximately $\Omega_{\rm i}t = 41$, the electron first encounters the shock and undergoes acceleration, which is indicated by the cyan panel and its corresponding color-matched sub-panel. During the phase of constant energy, the electron travels upstream, including the time when it is trapped by the non-linear structure. This suggests that the primary role of such structures is to confine electrons within the acceleration region. The last acceleration phase occurs during the electron's second encounter with the shock, highlighted with the salmon-pink color. The signature of SSDA is that the change in energy is directly proportional to the motional electric field. In our magnetic field configuration, electrons drift in the $+\hat{y}$ direction. From Panel (a), it can be observed that for the salmon-pink region, the predicted $\Delta\gamma$ (dashed black line) closely agrees with the measured values (solid red line), confirming the occurrence of SSDA during this acceleration stage. However, the presence of non-linear structures further complicates this picture, and the acceleration during the first phase of the sample electron cannot be fully described by SSDA. The cyan panel shows the measured $\Delta\gamma$ (blue solid line) and the analytical $\Delta\gamma$ (black dashed line) as a function of Δy for the first acceleration period. Although there are instances where the energization rate can be attributed to SSDA, $\Delta\gamma$ is also shown to increase for $\Delta y \leq 0$. This behavior is also evident in the subset of the most energetic traced electrons in Fig. 3(b). It indicates that they generally exhibit a linear relationship between $\Delta\gamma$ and Δy, similar to the sample electron shown in Figure 3 by the red circle. However, on average, the acceleration is about four times more efficient (dashed green line) than what can be accounted for solely from SSDA via the motional electric field (dashed purple line) [3].

The precise details of the underlying microphysics of the acceleration are likely a consequence of the complex non-linear structures arriving at the shock. Indeed, the non-linear structures arriving

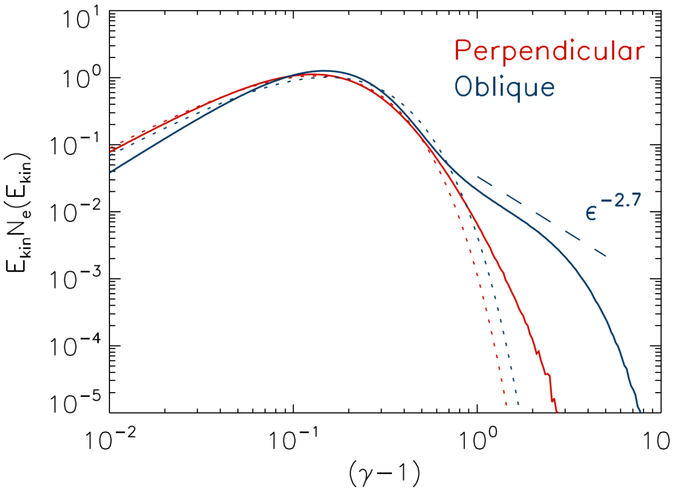

Figure 4: Downstream electron spectra for oblique (blue) and perpendicular (red) shocks.

at the shock also perturbate the local electric fields, with E_y/E_{0y} ranging from ±15 in the cyan region of Figure 3(a), yet averaging at $E_y/E_{0y} \approx 1$. The overall acceleration is therefore highly sensitive on local values and orientations of the electromagnetic fields.

5. Downstream electron distribution

Figure 4 illustrates the downstream electron distribution for both oblique and perpendicular ($\theta_{\rm Bn} = 90°$, [14]) shocks. Remarkably, the nonthermal electron population is much more prominent in oblique shocks, primarily due to the efficient acceleration via modified SSDA. High-energy electrons follow a power-law distribution with an approximate index of up to -2.7. The fraction of electrons not covered by the thermal distribution accounts for about 0.8% of the downstream electrons, yet they hold around 7% of the total downstream electron energy. The low-energy part of the spectra is represented by a Maxwellian distribution. The electron-to-ion temperature ratio is approximately $T_{\rm e}/T_{\rm i} = 0.17$, which closely aligns with the values observed in perpendicular shocks with similar shock parameters [15].

6. Conclusions

- The foreshock region exhibits both oblique waves with a magnetic component in the inner region and strong electrostatic fluctuations with k-vector along the x axis in the outer region. These waves are generated by the shock-reflected electrons streaming through the background plasma along the upstream magnetic field lines.

- The observed electron-beam instabilities agree very well with the predictions of a linear dispersion analysis, therefore, the electrostatic electron-acoustic instability dominates in the far upstream of the foreshock, while the denser electron beams in the near upstream drive the gyroresonant oblique-whistler instability.

- A number of mechanism contribute to electron acceleration in oblique shocks, such as reflection by electron-acoustic waves, capturing by nonlinear whistler waves and SSDA.
- SSDA produce the most energetic electrons and SSDA appears to be 4 times more efficient than theoretical prediction. We associate this high efficiency with the presence of nonlinear whistlers in the region where acceleration occurs.
- The downstream electron distribution exhibits a pronounced nonthermal population, resulting from efficient acceleration via modified SSDA. High energy electrons follow a power-law with an approximate index of -2.7.

Acknowledgments

A. B. was supported by the German Research Foundation (DFG) as part of the Excellence Strategy of the federal and state governments - EXC 2094 - 390783311. K.F. and M.P. acknowledge support by DFG through grant PO 1508/10-1. The numerical simulations were conducted on resources provided by the HPC system Raven at the Max Planck Computing and Data Facility and the North-German Supercomputing Alliance (HLRN) under projects bbp00033 and bbp00057.

References

[1] Bohdan, A., Weidl, M. S., Morris, P. J., et al. 2022, Physics of Plasmas, 29, 052301.

[2] Morris, P. J., Bohdan, A., Weidl, M. S., et al. 2022, ApJ, 931, 129.

[3] Morris, P. J., Bohdan, A., Weidl, M. S., et al. 2023, ApJ, 944, 13.

[4] Bohdan, A., Niemiec, J., Kobzar, O., et al. 2017, ApJ, 847, 1.

[5] Buneman, O., Computer Space Plasma Physics: Simulation Techniques and Software Eds.: H. Matsumoto & Y. Omura, Tokyo: Terra Scientific, 1993

[6] Niemiec, J., Pohl, M., Stroman, T., et al. 2008, ApJ, 684, 1174

[7] Buneman, O. 1958, PRL, 1, 8.

[8] Wu, C. S. 1984, GJR, 89, 8857.

[9] Leroy, M. M. & Mangeney, A. 1984, Annales Geophysicae, 2, 449

[10] Oka, M., Wilson, L. B., Phan, T. D., et al. 2017, ApJL, 842, L11.

[11] Katou, T. & Amano, T. 2019, ApJ, 874, 119.

[12] Matsumoto, Y., Amano, T., Kato, T. N., et al. PRL, 119, 105101.

[13] Oka, M., Otsuka, F., Matsukiyo, S., et al. 2019, ApJ, 886, 53.

[14] Bohdan, A., Niemiec, J., Pohl, M., et al. 2019, ApJ, 885, 10.

[15] Bohdan, A., Pohl, M., Niemiec, J., et al. 2020, ApJ, 904, 12.